INTERNATIONAL JOURNAL OF HYDROGEN ENERGY 46 (2021) 30959–30975

Available online at www.sciencedirect.com

ScienceDirect

journal homepage: www.elsevier.com/locate/he

H_2-rich syngas from glycerol dry reforming over Ni-based catalysts supported on alumina from aluminum dross

Nurul Asmawati Roslan [a], Sumaiya Zainal Abidin [a,b,*], Osarieme Uyi Osazuwa [c,f], Sim Yee Chin [a,b], Y.H. Taufiq-Yap [d,e]

[a] Department of Chemical Engineering, College of Engineering, Universiti Malaysia Pahang, Lebuhraya Tun Razak, 26300, Gambang, Kuantan, Pahang, Malaysia

[b] Centre for Research in Advanced Fluid & Processes (FLUID CENTRE), Universiti Malaysia Pahang, Lebuhraya Tun Razak, 26300 Gambang, Kuantan, Pahang, Malaysia

[c] Faculty of Chemical and Process Engineering Technology, College of Engineering Technology, Universiti Malaysia Pahang, Lebuhraya Tun Razak, 26300, Gambang, Kuantan, Pahang, Malaysia

[d] Catalysis Science and Technology Research Centre (PutraCAT), Faculty of Science, Universiti Putra Malaysia, 43400, UPM, Serdang, Selangor, Malaysia

[e] Chancellery Office, Universiti Malaysia Sabah, 88400, Kota Kinabalu, Sabah, Malaysia

[f] Department of Chemical Engineering, University of Benin, PMB 1154, Benin, Edo, Nigeria

HIGHLIGHTS

- Production of H_2-rich syngas from glycerol.
- Extraction of Al_2O_3 from aluminum dross waste.
- Ni-based catalyst supported on extracted Al_2O_3 was prepared.
- The effect of Ni loading, and reaction temperature are discussed in detail.
- Syngas with H_2:CO ratio less than 2.0 was obtained.

ARTICLE INFO

Article history:
Received 7 January 2021
Received in revised form
18 March 2021
Accepted 22 March 2021
Available online 22 April 2021

Keywords:
Ni-based catalyst
Alumina
Catalyst support
Glycerol

ABSTRACT

The performance of Ni-based catalyst supported on γ-Al_2O_3 for glycerol dry reforming (GDR) reaction was investigated in the current study. γ-Al_2O_3 was prepared from aluminum dross (AD) before use as catalyst support. Al_2O_3 was extracted using three different techniques assisted with ultrasonication: acid leaching with ammonia precipitation, acid leaching with re-precipitation of HCl, and alkaline leaching with ammonium hydrogen carbonate. The results show that extracted γ-Al_2O_3 3 (EGA3) with the highest purity and the surface area of 267.5 m^2 g^{-1} was produced from acid leaching with ammonia precipitation technique at a calcination temperature of 800 °C. A series of Ni/EGA3 (5%, 10%, 15% and 20%) catalysts were tested and it was found that the catalytic activity was increased in the order of 5%Ni/EGA3 < 10%Ni/EGA3 < 20%Ni/EGA3 < 15%Ni/EGA3. 15%Ni/EGA3 catalyst has the highest catalytic activity due to the excellent distribution of Ni on the EGA support, high specific surface area of the support and high catalyst's basicity. In addition, the strong Ni-EGA3 interaction of the 15%Ni/EGA3 catalyst suppressed the carbon formation with the

* *Corresponding author*. Department of Chemical Engineering, College of Engineering, Universiti Malaysia Pahang, Lebuhraya Tun Razak, 26300, Gambang, Kuantan, Pahang, Malaysia.
E-mail address: sumaiya@ump.edu.my (S.Z. Abidin).

https://doi.org/10.1016/j.ijhydene.2021.03.162

0360-3199/© 2021 Hydrogen Energy Publications LLC. Published by Elsevier Ltd. All rights reserved.

Dry reforming
Aluminum dross

catalyst having the lowest carbon deposition value of 25.51% during the GDR reaction carried out for 8 h. Studies on the GDR reaction catalytic activities revealed that 15%Ni/EGA3 achieved the maximum catalytic activity with 56.7% glycerol conversion, 44.7% H_2 yield, and 40.6% CO yield at 800 °C and CGR of 1:1. The H_2:CO ratio obtained in this study was approximately 1.2–1.5 throughout the reaction, depicting a relatively rich H_2 syngas product. Overall, the strong interaction between Ni and EGA3 ensured stable Ni particles that can mitigate carbon deposits, thereby enhancing the catalytic activity.

© 2021 Hydrogen Energy Publications LLC. Published by Elsevier Ltd. All rights reserved.

Introduction

In recent years, rapid growth in the biodiesel production by transesterification reactions has led to an excessive supply of glycerol by-product. Usually, biodiesel is produced from animal or vegetable-based oil. During this reaction, about 10% of glycerol is generated as a by-product [1]. This amount of glycerol is obviously in excess supply since glycerol has a low demand at less than 0.5 megatons [2]. This has led to increased studies on alternative glycerol conversion routes to more valuable products such as glycerol carbonate [3], which is well documented. Another very promising route that has aided the utilization of abundant glycerol is syngas production via glycerol reforming [4–6].

Syngas or synthetic gas, which mainly consists of H_2 and CO gas, can be produced from glycerol using many reacting agents (i.e., steam and CO_2 (dry)). Among these techniques, dry reforming of glycerol (GDR) has gained more attention due to the advantage of mitigating one of the abundantly available greenhouse gases via this route [7]. Reports have shown that the uncontrolled increasing emission of CO_2 into the atmosphere has led to critical environmental concerns [8] thus, making the glycerol steam reforming (GSR) route less favorable than GDR. Besides that, GDR reaction can produce H_2-rich syngas with H_2:CO molar ratio <2, thereby satisfying the feed conditions for Fischer-Tropsch (FT) synthesis [9,10]. Thus, the adoption of GDR as an alternative reforming route to produce H_2-rich syngas is more beneficial since H_2 is a major source of clean energy. The overall GDR reaction presented in Eq. (1) shows that to produce syngas, 1 mol of CO_2 was required for each mole of glycerol consumed [11,12].

$$C_3H_8O_3 + CO_2 = 4CO + 3H_2 + H_2O \quad \Delta H^{\circ} = 292\ \text{kJ/mol} \qquad (1)$$

It should be noted that in this process, catalysts are generally introduced to enhance the overall production of syngas and optimize the process. In the reforming process, two types of catalysts have been widely reported: noble-based and Ni-based catalyst. The application of noble metals (i.e., Pt, Rh) in reforming process was unfavorable due to their rarity and high cost, even though they were reported as very reactive and highly coke resistant catalyst [9,13,14]. The Ni-based catalyst has been reported to be a better option since it can produce similar catalytic activity at a lower price compared to the noble metal catalyst. Based on recent literature, the Ni-based catalyst is known to be a highly available, highly reactive, and cost-effective catalyst [15–18]. Ni is also known to have a high ability to breakdown C–C and C–H bonds, thereby promoting the water gas shift reactions and boosting H_2 and CO production [19,20]. However, the Ni catalyst commonly suffers from severe deactivation because of the sintering of Ni metallic clusters and high production of carbon during the reaction [21,22]. This has led to the introduction of catalyst support (i.e., ZrO_2, Al_2O_3) that can provide an alternative mechanism and reaction route to utilize the deposited carbon and eradicate metal sintering [23]. Strong interaction between active metal and support could reduce the carbon formation and promote catalyst's stability and reducibility [24].

The support selection is generally dependent on the physicochemical properties that are to be enhanced (i.e., surface basicity, thermal stability, oxygen storage capacity, pore characteristics and surface area). These properties will prevent catalyst sintering, increase active particles' dispersion, provide better interaction between metal and support, facilitate catalyst reduction, and provide alternative carbonaceous species routes [25,26]. One outstanding catalyst support combination that is commonly utilized for hydrocarbon-based reforming is Ni catalysts supported on Al_2O_3 [27–29] This catalyst is known to possess high surface area, small pores, high ability to inhibit catalyst sintering, and good metal dispersion, Al_2O_3 as catalyst support ensures the synthesized catalyst remains thermally stable even at high reaction temperature. Hence, it is responsible for the additional mass transfer limitation experienced by the reactants [30–33].

Until recently, Al_2O_3 is extracted from bauxite by the Bayer process, which requires a complicated extraction technique at high cost. A unique and cheaper alternative route to obtain high purity Al_2O_3 can be achieved via the extraction of alumina from aluminium wastes and scraps. Aluminum dross (AD), a waste produced from the aluminium industry has a high content of Al_2O_3, approximately around 60–90% depending on the type of dross [34,35]. AD is formed on a molten aluminum surface exposed to high temperatures in the furnace during primary and secondary processes. The aluminum industry generates $>1 \times 10^6$ tons/annum of AD and approximately 95% of it was dumped in the factories vicinity [36]. Usually, the dross was discarded in landfills which poses hazard to the environment [37]. Several value-added products such as hydrotalcite [38], AD-derived concrete blocks [39], and mullite-zirconia composites [40] are produced and extracted from AD to achieve zero hazardous waste. Due to the high content of Al_2O_3 in AD with different phases (i.e., α, β, and γ), research on the extraction of Al_2O_3 from AD has been extensively investigated and reported in literature [41–43]. Since these Al_2O_3 from AD

shows favorable and comparable properties, it could be extensively used in many industries (i.e., medical, ceramic) to replace the conventional Al_2O_3. Interestingly, the utilization of extracted Al_2O_3 from AD for catalysis has not well been established in literature. Also, reports on the application of extracted products from AD is still lacking, especially in areas such as preparation techniques, physicochemical properties, and preliminary studies of the products.

Therefore, this study focuses on the production of Al_2O_3 from AD and further utilization as a catalyst support in the GDR reaction. The research is divided into three stages, (i) the extraction and characterizations of Al_2O_3 from AD; (ii) the preparation and characterizations of Ni catalyst supported on extracted Al_2O_3, and (iii) the catalytic evaluation in GDR reaction. Herein, Al_2O_3 was produced from three different techniques: acid leaching with ammonia precipitation, acid leaching with re-precipitation of HCl, and alkaline leaching with ammonium hydrogen carbonate. A modification has been made for those three techniques by introducing an ultrasonication process during Al_2O_3 preparation to enhance the separation process and therefore increase the specific surface area. Then, the metal-support interaction between Ni (at 5%, 10%, 15%, and 20%) and extracted Al_2O_3 was investigated to evaluate the performance of Ni catalyst and extracted Al_2O_3 in the GDR reaction (i.e., catalytic evaluation and stability test). Previously, our research team prepared Ni-based catalyst by wet-impregnation technique using extracted Al_2O_3 as a catalyst support [44]. Due to low catalytic performance in the previous study, a current work introduced an ultrasonication-assisted technique during the catalyst's preparation to enhance the catalyst's surface area and metal-support interaction. In addition, the correlations between catalytic performance and physicochemical characteristics of the synthesized catalysts were elucidated. Based on the current state of research in reforming, this study establishes a unique work, which combines the production of Al_2O_3 from AD, which was further used in the development of Ni-based Al_2O_3 catalyst for the recovery of H_2-rich syngas from GDR.

Experimental

Materials

AD was obtained from a waste collection center in Malaysia. Hydrochloric acid (37%), sulphuric acid (98%), sodium hydroxide (99%) and ammonium hydrogen carbonate (99%) were purchased from Sigma Aldrich, Malaysia. Meanwhile, ammonia solution (30%) and nickel (II) nitrate hexahydrate (99%) were supplied by Merck, Malaysia.

Experimental procedure

The experimental work is divided into three main stages, which are: (a) preparation and characterizations of extracted Al_2O_3, (b) preparation and characterizations of Ni-based catalyst supported on extracted Al_2O_3, and (c) catalytic evaluation in GDR reaction.

Preparation of extracted Al_2O_3

Extracted Al_2O_3 (EA) was prepared by three different techniques, which are: (i) acid leaching with ammonia precipitation, (ii) acid leaching with re-precipitation of HCl, and (iii) alkaline leaching with ammonium hydrogen carbonate. The procedure for the acid leaching method was adopted from a study by How et al. [45]. Meanwhile, the acid leaching with re-precipitation of HCl method was originally adopted from a study by Mahinroosta et al. [46] and alkaline leaching with ammonium hydrogen carbonate method was adopted from Miskufova et al. [47]. A slight modification using the ultrasonication process was introduced into these three techniques. Details of these methods can be found in the supplementary data. The Al_2O_3 extracted from acid leaching with ammonia precipitation, acid leaching with re-precipitation of HCl and alkaline leaching with ammonium hydrogen carbonate were denoted as EA1, EA2 and EA3, respectively.

Preparation and characterizations of Ni-based catalyst supported on extracted Al_2O_3

In the current study, a Ni-based catalyst supported on EA was synthesized via the ultrasonicated impregnation method. Firstly, Ni $(NO_3)_2 \cdot 6H_2O$ (Merck, ≥98%) was accurately weighed (i.e., 0.2 g) and dissolved in distilled water for about 5 min. The solution was placed in a beaker containing 1 g of extracted Al_2O_3 and placed for 4 h in an ultrasonication water bath (i.e., 80 °C). The resulting product was dried (110 °C, 12 h) before calcined for 5 h at 950 °C. The sample was denoted as 5 %Ni/Al_2O_3. The same technique was employed to synthesize all the X%-Ni/Al_2O_3 catalyst (with X = 5, 10, 15, 20). The samples were further characterized by X-ray diffraction (XRD), CO_2- temperature programmed desorption (CO_2-TPD), transmission electron microscopy (TEM), X-ray photoelectron spectra (XPS), BET surface area, and H_2 temperature programmed reduction (H_2-TPR).

Catalytic evaluation in GDR reaction

GDR reaction was conducted in a fixed-bed reactor for 8 h time-on-stream (TOS). The reactor tubing with length, L = 30 cm and internal diameter, ID = 0.95 cm, was vertically positioned in a furnace. 0.2 g of the prepared catalyst was weight and placed in the middle of the reactor tube. Before the reaction, H_2 gas (9.9 ml min^{-1}) was introduced to reduce the catalyst for 1 h at 700 °C. Then, the reactant gas (i.e., CO_2) and glycerol were fed into the reactor. The outlet gas passed through a drierite bed to remove humidity before it was collected for analyses. The product was analyzed using Agilent 6890 gas chromatography (GC). The glycerol conversion H_2 yield, and carbon-containing species were calculated using Eqs. (2)–(4).

Glycerol conversion:

$$X_G = \frac{2\ F_{H_2} \times 4F_{CH_4}}{8\ F_{C_3H_8O_3}} \times 100 \quad (2)$$

Hydrogen yield:

$$Y_{H_2} = \frac{2\ F_{H_2}}{8\ F_{C_3H_8O_3}} \times 100 \quad (3)$$

The yield of carbon-containing species

$$Y_i = \frac{F_i}{3 \times\ F_{C_3H_8O_3}} \times 100 \quad (4)$$

where i = CO, CO_2, and CH_4, F_i = outlet flow rate.

Results and discussion

Characterizations of EGA

(a) X-ray fluorescence

Table 1 represents the XRF analysis of AD, EA1, EA2, and EA3. All the extracted Al_2O_3 have a purity of more than 97 wt%. The results show that EA1 synthesized by acid leaching with ammonia precipitation has the highest purity with 100 wt% Al_2O_3. Meanwhile, for the second and third extraction techniques, EA2 and EA3 have Al_2O_3 purity of 98.4 wt% and 97 wt%, respectively, with the presence of SiO_2 traces. According to Mahinroosta et al. [48], Species of $Si(OH)_4$ are contained in aluminum hydroxide precipitate residue after EA extraction. At high calcination temperature (i.e., >200 °C), the removal of physiosorbed water from Si $(OH)_4$ species occurred. In addition, at high temperature, any remaining silanol species will be condensed by removal of water particle [49]. Thus, the remaining SiO_2 will remain as an impurity in the extracted products. The reaction represented in Eq. (5) occurred as follows.

$$Si(OH)_4 = SiO_2 + 2H_2O \quad (5)$$

Table 1 – AD and EA compositions obtained from XRF analysis.

Chemical compositions	AD (wt.%)	EA1 (wt.%)	EA2 (wt.%)	EA3 (wt.%)
Al_2O_3	64.7	100	98.4	97
CO_2	10.8	–	–	–
N_2	9.58	–	–	–
SiO_2	3.36	–	1.6	3
B_2O_3	3.22	–	–	–
Fe_2O_3	2.06	–	–	–
MgO	1.92	–	–	–
Na_2O	1.07	–	–	–
Cl	0.387	–	–	–
CuO	0.271	–	–	–
TiO_2	0.236	–	–	–
SO_3	0.151	–	–	–
Others	2.245	–	–	–

The chemical reaction that occurred during these three extraction techniques are presented in supplementary data.

(b) X-ray diffraction

The X-ray diffractogram (XRD) of AD, EA1, EA2, and EA3 are shown in Fig. 1. The diffractogram depicts the presence of various elements in AD such as Al (JCPDS No: 00-004-0787), Al_2O_3 (JCPDS No: 00-042-1468), MgO (JCPDS No: 00-004-0829), spinel $MgAl_2O_4$ (JCPDS No: 00-005-0672), SiO_2 (JCPDS No: 00-046-1045), aluminum nitride (AIN) (JCPDS card No: 00-025-1133), NaCl (JCPDS No: 00-005-0628), Fe_2O_3 (JCPDS No: 00-039-1346) and KCl (JCPDS No: 00-004-0587). Meanwhile, the XRD results of EA1, EA2, and EA3 confirm the presence of γ-Al_2O_3 in each sample at 2θ = 19.8°, 32.9°, 36.4°, 39.1°, 45.9°, 61.3°, and 67.3° (JCPDS No: 00-029-0063) which corresponded to (311), (400) and (440) planes. Additional peak which indicates the existence of SiO_2 species are observed at $2\theta = 42.8°$ (JCPDS card No: 00-046-1045) for EA2 and EA. These XRD analyses corroborated with the XRF data tabulated in Table 1. In agreement with this study, How et al. [45] also reported that γ-Al_2O_3 is produced when AD is calcined at 900 °C and pH between 5 and 9.

(c) Textural properties (BET)

The textural properties of AD and EA is tabulated in Table 2. There is a significant increment in the BET surface area when EA was extracted from AD. The low surface area of the AD was due to pore blockage by metals on the Al_2O_3 surface. Various metals in the AD block the pore of Al_2O_3 and therefore reduced the surface area. The main element in EA after the extraction process was γ-Al_2O_3 with no significant presence of trace metals. Almost all metals were eliminated from the Al_2O_3 surface. The BET surface area of EA1 was highest at 163.51 $m^2\ g^{-1}$, while EA2 and EA3 had 126. 35 $m^2\ g^{-1}$ and 119.25 $m^2\ g^{-1}$, respectively. However, the average pore diameter of AD was much higher compared to all synthesized EA because of the aggregation and formation of various metals on porous structure of the Al_2O_3. According to the IUPAC sorption isotherms, all the synthesized EA exhibits type H2 hysteresis loop from type IV curve. This type of isotherm represents the mesoporosity of the synthesized material. In addition, type H2 hysteresis loop suggests that mesoporous particles undergoes

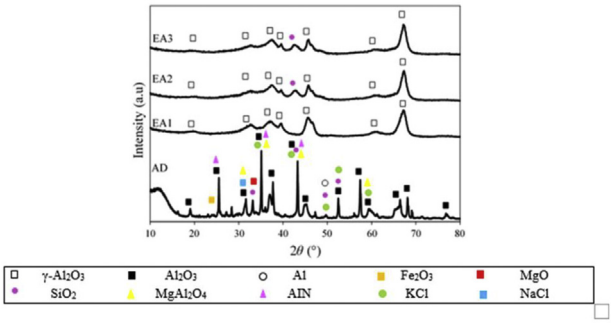

Fig. 1 – X-ray diffractograms of AD, EA1, EA2, and EA3.

Table 2 – Properties of AD and EA.

Particles	BET surface area ($m^2\ g^{-1}$)	Average pore volume ($cm^3\ g^{-1}$)	Average pore diameter (nm)	The crystallite size (nm)[a]
AD	8.00	0.23	61.47	7.80
EA1	163.51	0.62	15.6	5.57
EA2	126.35	0.56	15.2	5.60
EA3	119.25	0.51	14.7	5.63

[a] Crystallite size of Al_2O_3 phase calculated using the most intense Al_2O_3 line at 2θ of 67.3° (i.e. correspond to plane (440)) using Scherer Equation.

a capillary condensation phenomenon [50]. The adsorption-desorption isotherms and pore size distribution of the AD and all prepared EA were presented in the supplementary data. The crystallite size was around 5 nm for all synthesized EA. The larger crystallite size of AD (i.e., 7.8 nm) was observed probably due to the presence of various Al_2O_3 phases. The calculated crystallite size obtained in this study can be classified as a nanocrystalline powder, and it is comparable with commercialized Al_2O_3.

(d) Field emission scanning electron microscopy

The morphology of AD and as-synthesized EA is illustrated in Fig. 2. The morphology of AD with several particles' shapes such as rounded-corner-shaped and long stick-shaped, indicates the existence of various metals on the Al_2O_3 surface. Fig. 2(b–d) show a smoother surface. More specifically, Fig. 2(b) shows the consistent flake-like shape particles, indicating the presence of Al_2O_3 [51,52]. The morphology of the EA2 and EA3 shows small spherical-like particles with dense agglomerates on the particle's surface. These particles are from impurities of SiO_2, as previously discussed in the XRD and XRF analyses. Similar morphology of SiO_2 under FESEM analysis was also found by Hindryawati et al. [53]. The spherical-like SiO_2 particles with clumpy shape was consistent with findings from this study. The smoothest surface of EA1 had the highest surface area (clear pore), and the messy surface of AD indicated the presence of various metals on the EA surface, resulting in lower surface area.

Effect of calcination temperature

EA1 with the highest Al_2O_3 content was selected for the studies on the effect of calcination temperature. The study was conducted based on the characterization studies from the XRD and BET surface area analysis. The experimental work centers on determining the type and presence of alumina phases in the extracted samples and ensuring the alumina structure are consistency at different operating temperatures. Also, this study was carried out to prove that gamma alumina was stable at the investigated reaction temperature (800 °C). Eq. (6) represents the reaction that occurs during the calcination process.

$$2Al(OH)_3(S) = Al_2O_3(S) + 3H_2O(l) \quad (6)$$

Four calcination temperatures with a heating rate of 5 °C min^{-1} were introduced, i.e., 600 °C, 700 °C, 800 °C, and 900 °C. The synthesized γ-Al_2O_3 at 600 °C, 700 °C, 800 °C, and 900 °C calcination temperature was denoted as EGA1, EGA2, EGA3 and EGA4, respectively. Since EGA3 showed the highest specific surface area, it was used in this study as catalyst support in GDR reaction. Details of the effects of calcination temperature can be found in the supplementary section.

Characterizations of Ni/EGA3

Four catalysts with different loading were prepared to investigate the interaction between Ni (metal) and as-synthesized EGA3 (support).

(a) X-ray diffraction

The diffractogram of calcined EGA3 as catalyst support and synthesized Ni/EGA3 catalyst are presented in Fig. 3. The presence of γ-Al_2O_3 is detected in each sample at 2θ = 19.8°, 32.9°, 37.4°, 39.6°, 45.9°, 61.3° and 67.3° (JCPDS No: 00-029-0063). The addition of Ni into the EGA3 support produced two additional peaks; NiO at 2θ = 37.4°, 43.5° and 63.3° (JCPDS No: JCPDS card No: JCPDS 01-073-1519) and spinel $NiAl_2O_4$ at 2θ = 37.4° and 75.5° (JCPDS No: JCPDS 00-010-0339). The spinel phase formation possesses strong metal-support interaction because of the high calcination temperature employed [54]. As presented in Fig. 3, the peak intensity was increased when Ni loading increased from 5 to 20% Ni/EGA3. This was indicative

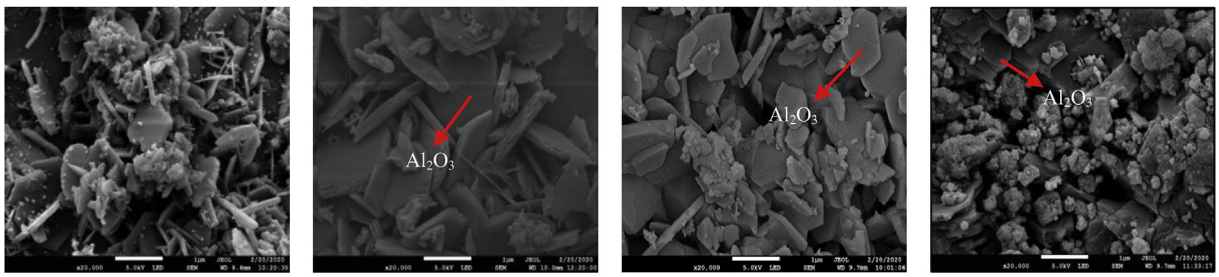

Fig. 2 – FESEM image of (a) AD, (b) EA1, (c) EA2, and (d) EA3 at 20 k magnification.

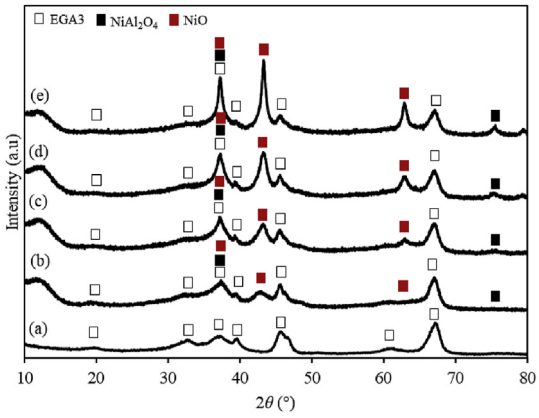

Fig. 3 – X-ray diffractograms of (a)EGA3, (b)5%Ni/EGA3, (c) 10% Ni/EGA3. (d)15%Ni/EGA3 and (e)20%Ni/EGA3.

of more NiO species which existed on the exterior surface of EGA3 support at higher loading of Ni. This data was consistent with the findings reported by Shafiee et al. [55] They reported that the high peak intensity of the NiO as Ni metal loading increased was indicative of larger metal deposited on the catalyst's surface.

The crystallite size of NiO for all the synthesized catalyst were calculated via Scherrer equation at $2\theta = 43.5°$ as tabulated in Table 3. Referring to the tabulated data, the NiO's crystallite size increased with the addition of Ni in the order 5%Ni/EGA3 (11.53 nm) < 10%Ni/EGA3 (12.59) < 15%Ni/EGA3 12.63 nm) < 20%Ni/EGA3 (12.77). These results indicate a good metal dispersion at lower Ni loading. Larger crystallite size of 20%Ni/EGA3 was probably due to the suppression of Ni ions migration into the EGA3 structure, which limits the Ni-EGA3 interaction. This result was in conformity with previous study by Takenaka et al. [56] which reported a decrement in NiO dispersion with an increment of NiO crystallite size. Nevertheless, the crystallite sizes for all catalysts were still smaller than the support pore diameter, indicating a well-dispersed metal on the support surface.

(b) Textural properties (BET)

The physical properties of EGA3 and Ni/EGA3 catalyst employed in GDR reaction are tabulated in Table 3. EGA3 prepared at 800 °C calcination temperature possessed the highest BET surface area of 267.53 $m^2\ g^{-1}$. Addition of NiO's led to a reduction in the BET surface area from 267.53 $m^2\ g^{-1}$ to 143.14 $m^2\ g^{-1}$, indicative of the successful diffusion of active metals on the surface of the catalyst. This is because of the partial pore blockage by NiO metal diffusion into EGA support's porous surface. The average pore diameter of the EGA3 support has increased slightly with the introduction of Ni metal. This could be due to the decomposition of Ni $(NO_3)_2$ during the calcination process which results in the development of Ni/EGA3 with lower number of pores and higher pore diameter. Nevertheless, the catalyst's pore volume was still lower than the supporting material. The adsorption-desorption isotherms and pore size distribution of all synthesized catalysts were presented in the supplementary data.

(c) Transmission electron microscopy

The surface morphologies of the EGA3 and synthesized Ni/EGA3 catalysts are shown in Fig. 4. The Ni metal appeared as small dark dots, while EGA3 support was detected as a grey surface. The existence of the dark spot was seen in Fig. 4(b)–(e), indicative of the existence of Ni metals on the EGA3 surface. As the loading increased, many dark spots were seen on the surface of the EGA3. This shows that Ni was dispersed well on the EGA3 support surface. The presence of ultrasonic waves during the preparation technique drives the uniformity of Ni collision with EGA3, thereby plugging Ni particles into the channels of EGA3 support. There is a correlation between these findings and the XRD analysis, where larger Ni particle size was observed at higher Ni loadings. In comparison with other synthesized catalysts, 15%Ni/EGA3 catalyst represented in Fig. 4(d) shows the most consistent Ni dispersion and uniform particle size. For 20%Ni/EGA3, a few agglomeration spots were spotted on the EGA3 surface which resulted in larger particle size of Ni (i.e., 12.7 nm).

(d) X-ray photoelectron spectroscopy

Fig. 5 shows the X-ray photoelectron spectra of all synthesized catalysts. The Ni $2p_{3/2}$ binding energy of 855 eV was observed for 5%Ni/EGA3, 10%Ni/EGA3, and 20%Ni/EGA3. Whereas, for 15%Ni/EGA3, the peak shifted slightly to 857 eV. This binding energy obtained was described as oxidation state of Ni^{2+} [57], which agrees with the study by Peck and Langell [58]. The study stated that the standard Ni $2p_{3/2}$ located at 854 and 857.2 eV was ascribed to pure NiO and spinel $NiAl_2O_4$ phases, respectively. Moreover, it correlates well with the XRD analysis obtained in this study, which showed the presence of

Table 3 – Properties of EGA3 and Ni/EGA3.

Particles	NiO crystallite size (nm)		BET surface area ($m^2\ g^{-1}$)	Average pore volume ($cm^3\ g^{-1}$)	Average pore diameter (nm)
	Fresh[a]	Spent[b]			
EGA3	–	–	267.53	0.85	16.2
5%Ni/EGA3	11.53	13.81	230.79	0.79	17.5
10%Ni/EGA3	12.59	13.73	210.81	0.75	18.0
15%Ni/EGA3	12.63	13.11	165.36	0.64	18.3
20%Ni/EGA3	12.77	13.22	143.14	0.56	18.9

[a] Crystallite size of NiO calculated using the most intense NiO line at 2θ of 43.5°.
[b] Crystallite size was measured using TEM.

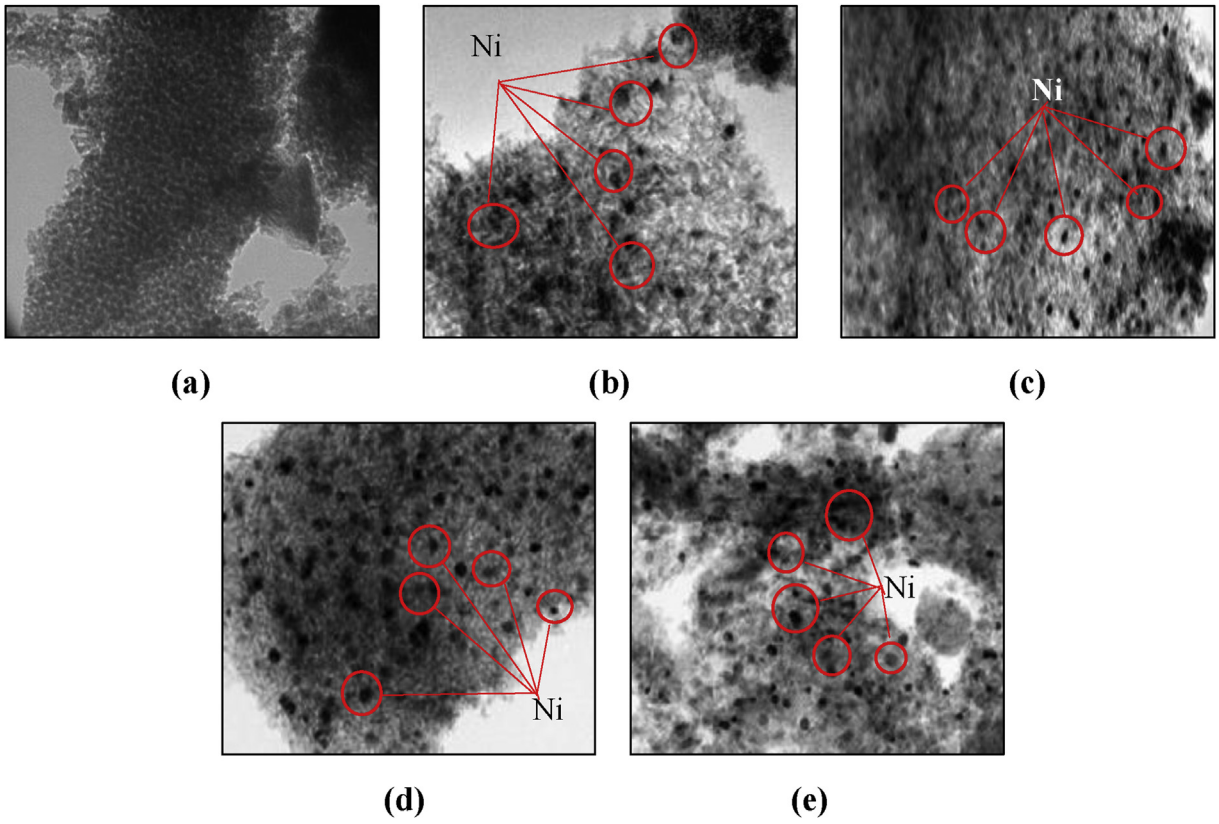

Fig. 4 – TEM images of (a)EGA3, (b)5%Ni/EGA3, (c)10%Ni/EGA3, (d)15%Ni/EGA3 and (e)20%Ni/EGA3.

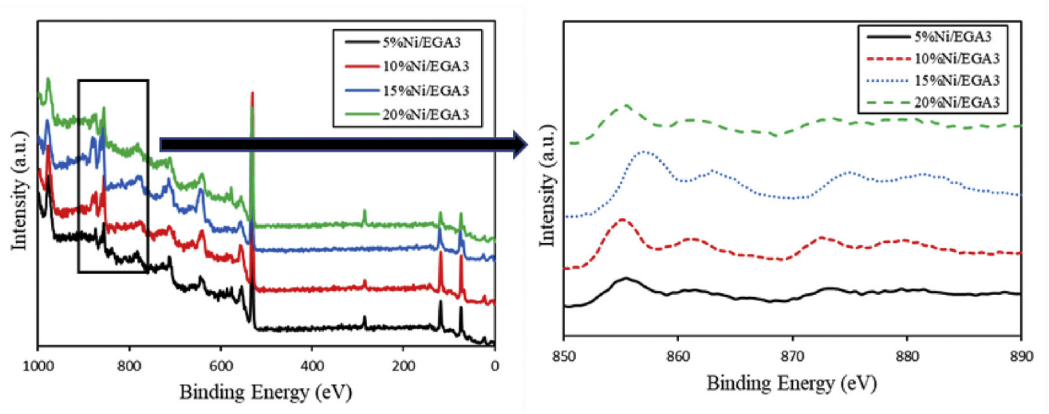

Fig. 5 – XPS spectra of fresh catalysts.

NiO and $NiAl_2O_4$. Based on the result, 15%Ni/EGA3 possesses the highest binding energy for Ni $2p_3$ peak, suggesting that the NiO particles and EGA3 support had a strong interaction. The intense binding energy is due to the small Ni particle size, where it can promote its interaction with EGA3 support. However, when 20% Ni loading was employed, results demonstrated that Ni loading varied inversely with the binding energy. This was because the quality of metal-support interaction significantly dropped due to excess supply of Ni particles. Excess of Ni metals produced larger Ni particles which do not support uniform dispersion therefore, resulting in the sintering of the tightly bonded Ni particles. In addition, the available surface area of the support was insufficient for proper metal support interaction. This resulted in the agglomeration of metal particles during synthesis and weaker bond formation which led to reduction in the binding energy.

(e) CO_2 temperature-programmed desorption

CO_2-TPD profile represented in Fig. 6(a) shows three distinct peaks of EGA3 support and Ni/EGA3 catalysts, indicating three types of basic sites. The low-temperature peak between 50 and 150 °C indicates weak basic sites, which represents the removal of adsorbed moisture. The peak

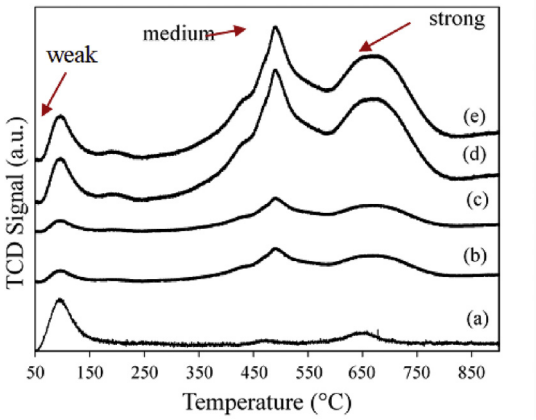

Fig. 6 – CO2-TPD profile of (a) EGA3, (b) 5%Ni/EGA3, (c) 10% Ni/EGA3, (d) 15%Ni/EGA3 and (e) 20%Ni/EGA3.

appearing between 450 and 600 °C represents medium basic sites. Meanwhile, peak found between 600 and 800 °C indicates the strong basic sites which depicts adsorption on low coordinates of O^- sites [59]. A summary of the amount of CO_2 desorbed from the catalyst's surface is presented in supplementary data. 15%Ni/EGA3 shows the highest value of CO_2 desorbed (i.e., 199.6 μmol g^{-1}) and the highest amount of strong basic site with a value of 108 μmol g^{-1}. This result indicates that 15%Ni/EGA3 catalyst has the highest capacity to adsorb acidic CO_2 onto its surfaces compared to the other catalysts. This could reduce the carbon formation during the reaction [60] and thus increase the catalytic performance. For the 20% Ni loading catalyst, a drop in CO_2 adsorption capacity was observed. During the catalyst synthesis, the amount of Ni nanoparticles outnumbered the active support surface area available for metal-support interaction. Therefore, the excess Ni metals agglomerate and formed larger particles which do not support uniform dispersion. The agglomerated Ni particles caused by insufficient support surface (due to excess supply of 20%Ni) resulted in agglomeration and sintering during synthesis, hence reducing the overall efficiency of the

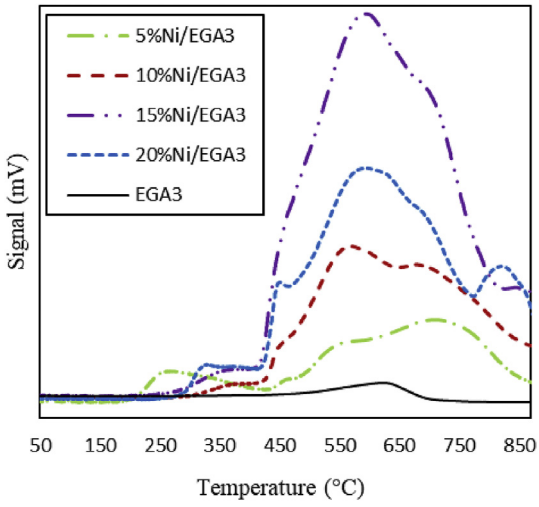

Fig. 7 – H_2-TPR of EGA3, 5%Ni/EGA3, 10%Ni/EGA3, 15% Ni/EGA3, and 20%Ni/EGA3.

catalysts. Hence, the CO_2 adsorption capacity of the 20% Ni catalyst drop.

(f) H_2 temperature-programmed reduction

The TPR profile of the pure Al_2O_3 represented in Fig. 7 is flat, which indicates its inertness towards reduction of H_2. The reduction of NiO particles with H_2 as a reducing agent is widely reported as a single step for converting NiO to the metallic Ni phase [61]. Fig. 7 shows the results of H_2-TPR for all samples, and from the result, three reduction peaks are seen. The peaks appeared at temperature range of 200–450 °C while 550–650 °C presents the reduction of NiO species to Ni° metallic phase with weak interaction between support and metal [62,63]. The third peak located at a reduction temperature range of 650–900 °C was ascribed to the reduction of NiO particles located in the bulk EGA support. (i.e., Eq. (7)).

$$NiO+H_2=Ni+H_2O \quad (7)$$

Therefore, approximately 700 °C was selected as the catalyst reduction temperature to ensure all NiO species located on the catalyst surface are reduced to Ni° metallic phase. According to Oemar et al. [64], the reduction temperature of NiO also depends on the strength between metal and support (i.e. metal-support interaction). Based on the H_2-TPR profile represented in Fig. 7, as the loading of Ni increases, the reduction temperature of NiO phase shifts to a higher temperature region, thereby increasing the metal-support interaction. The higher metal-support interaction for Ni-based catalysts resulted from uniform dispersion of smaller NiO crystallite size on the surface of the EGA3 support. However, at 20%Ni/EGA3, NiO's reduction was lower, and the reduction of spinel $NiAl_2O_4$ was at its highest. This is probably because of the lower thermal stability and weaker metal-support interaction exhibited by the 20%Ni/EGA3 when compared to the 15%Ni/EGA3 catalyst.

Catalytic evaluation of GDR reaction

Nickel loading

The catalytic activity of the Ni/EGA3 catalyst in GDR was conducted for 8 h time-on-stream (TOS), CO_2 to glycerol ratio (CGR) of 1, WHSV = 3.6×10^{-4} $mlg^{-1}h^{-1}$ STP and 700 °C reaction temperature. Four different loadings were evaluated to investigate the interaction between Ni metallic particle and EGA3 support: 5%Ni/EGA3, 10%Ni/EGA3, 15%Ni/EGA3, and 20% Ni/EGA3. The reaction performance parameters which include, glycerol conversion, products yield (i.e., CO and H_2) and ratio of H_2 to CO (H_2:CO) are represented in Fig. 8. This section will discuss the catalyst behavior at different loadings to fully comprehend the effect of Ni metal loading and its interaction with EGA3 support. Results from the study showed that Ni loading varied directly with glycerol conversion, from 5% to 15% and then an inverse relationship is observed from 15% to 20% (Fig. 8(a)). During the CO_2 glycerol reforming reaction, the metallic catalyst (e.g., Ni) can either be affected by excess carbon deposits or metal sintering. According to Luisetto et al. [65], Ni-based catalyst is very active, but they are

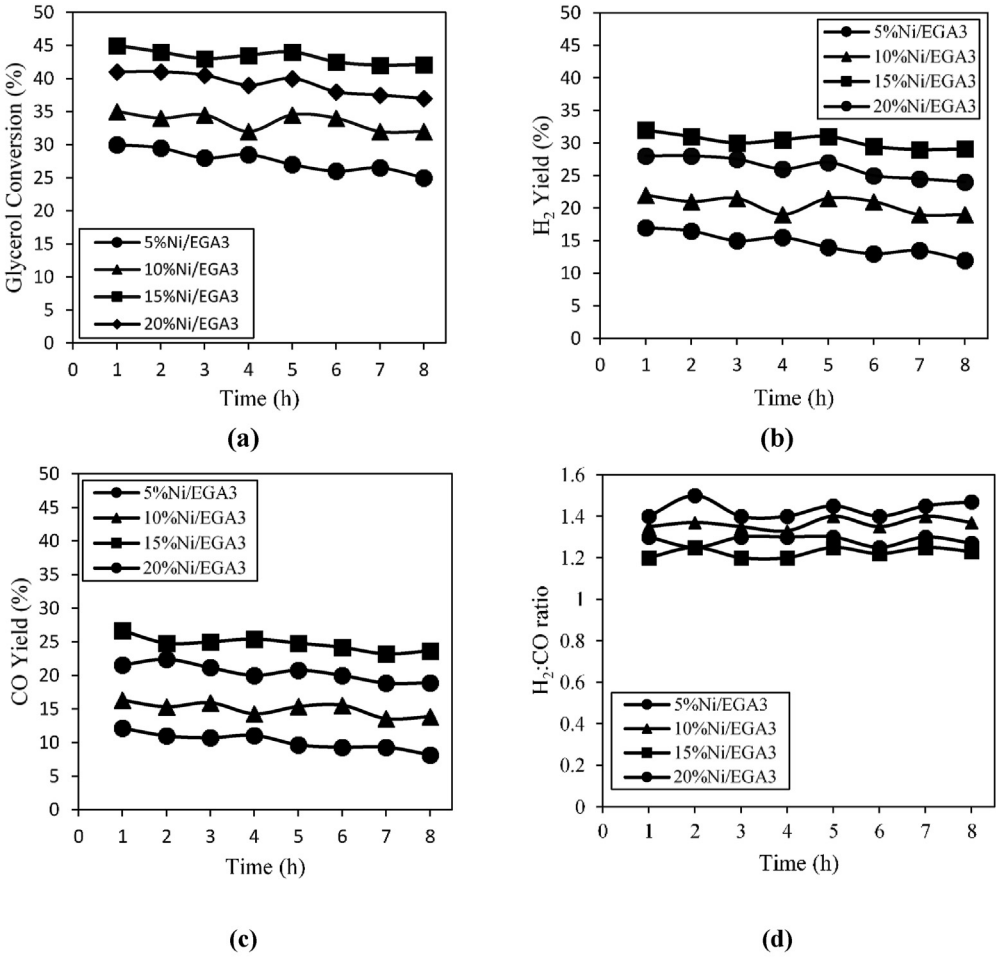

Fig. 8 – Effect of catalyst loading on (a)Glycerol conversion, (b)H2 yield, (c)CO yield, and (d)H2:CO ratio.

prone to carbon attacks due to their ability to breakdown C–H bonds, which are present in hydrocarbons such as glycerol.

(a) Glycerol dry reforming over 5%Ni/EGA3

At low Ni loading (5%), Ni availability is limited at the catalyst surface. As reactants are continuously supplied to the reaction, the limited available Ni at the surface is not sufficient to break large amount of glycerol during the reforming reaction. Therefore, a sizeable amount of glycerol remains unconverted over 8 h TOS. The glycerol conversion, H_2 yield and CO yield achieved was 26%, 13% and 8%, respectively. Nonetheless, studies by Bac et al. [11] revealed that 5 wt % was the optimum Ni loading (from comparative studies carried out at 1, 5 and 10 wt% metal loading) for Ni/AZT catalyst in the GDR reaction. Ni loading greater than 5 wt% had inhibiting effects on the metal dispersion; a condition also reported by Koc and Avci [66]. However, this finding is not in agreement with our study probably due to the outstanding effect of the EGA3 support which provided larger surface area for more Ni nanoparticle to be embedded and interact with C–H bonds thereby resulting in better cracking of glycerol and catalytic performance. Furthermore, at this Ni loading (5%), sintering is not observed during reaction because the support provides sufficient surface area for the metal to be dispersed; hence, agglomeration which leads to metal sintering did not occur.

(b) Glycerol dry reforming over 10%Ni/EGA3

At 10% Ni loading, the catalyst performance increased slightly. The glycerol conversion, H_2 and CO yield were 32%, 19% and 13%, respectively. The slight increment could be due to the availability of more Ni metals at the surface to fill up vacant pores in the EGA3 support. Therefore, with the increased availability of Ni particles, more C–H bonds are cracked at the surface, leading to higher conversion and product formation rate. Although available data from this study is insufficient to prove this, there could also be the possibility of increased catalyst stability when comparing longevity at 5 and 10% Ni/EGA3 catalyst. This is because more Ni particles are available to interact with the EGA3 support, thereby forming a strong catalytic pair required to convert the hydrocarbon species. It is expected that the catalyst longevity is dependent on the ability of the catalytic surface to constantly remain free from either hydrocarbon or carbon species. Although, literature on glycerol CO_2 reforming using 10 wt%Ni catalyst is scarce, several researchers have used 10% Ni catalyst for hydrocarbon steam reforming. For instance,

Feng et al. [67] used 10% Ni/CaO-modified attapulgite for the production of H_2 in steam reforming of glycerol. The authors obtained glycerol conversion and H_2 yield of 93.71% and 85.30%, respectively. This was attributed to improved metal dispersion which aided the water-gas-shift (WGS) reaction, thereby increases the H_2 yield. Ismaila et al. [15] used 12%Ni on Ce-modified γ-Al_2O_3 to obtain conversion of glycerol and H_2 yield of ca.77% and ca.62%, respectively. Moreover, Ni loading between 8 and 16% has majorly been employed by researchers for Ni catalysts formations to avoid metal agglomeration, which could lead to sintering in-situ reaction [15].

(c) Glycerol dry reforming over 15% Ni/EGA3

A significant increase was observed in the catalyst performance when the Ni loading on Ni/EGA3 was increased to 15%. Glycerol conversion, H_2 and CO yield were 42%, 29% and 23%, respectively. This means that there is a direct relationship between performance and Ni loading during the reaction process. The EGA3 support provided the required surface area for the Ni nanoparticle to be uniformly dispersed on. Also, the increased activity can be linked to sufficient availability of Ni particles at the surface (due to increased supply of Ni particles at 15%), to breakdown C–H bonds supplied by the glycerol feedstock which is known to have long hydrocarbon chain. Hence, catalyst deactivation was highly controlled as there was good interaction between the reactants flowing into the reaction and the active Ni sites which were well dispersed on the EGA3 support. This led to continuous breakage of C–H bonds and conversion of reactants to products. Apart from the catalyst's deactivation due to the carbon deposition, sintering from agglomeration of metal species can also hinder the effectiveness of the catalyst in GDR. At 15%Ni catalyst loading, due to increasing catalytic performance over the time-on-stream, it can be deduced that the amount of sintering was negligible or not significant. Therefore, the metal loading was adequate for uniform dispersion on the available support surface area.

Interestingly, all characterizations carried out supports the higher performance of the 15%Ni/EGA3 catalyst. For instance, TEM images represented in Fig. 4 showed that 15% Ni/EGA3 catalyst was the most consistent in terms of Ni dispersion and uniformity of the particle size. XPS spectra (refer to Fig. 5) representing all Ni catalysts with different loading showed that the peak representing the Ni $2p_{3/2}$ in 15% Ni/EGA3 had shifted to higher binding energy of 857 eV, whereas other catalysts had binding energy of 855 eV. According to Arcotumapathy et al. [57], and Peck and Langell [58], this binding energy represents the oxidation of Ni^{2+}. These results suggest strong NiO - EGA3 support interaction and adequate surface area for uniform metal particle dispersion. Ni loading also varied directly with the reduction temperature of NiO phase, thereby, increasing the metal-support interaction. CO_2-TPD represented in Fig. 6 showed that 15%Ni/EGA3 had the highest amount of CO_2 desorbed (199.6 $\mu mol\ g^{-1}$) and the highest amount of strong basic site (108 $\mu mol\ g^{-1}$). The basicity possessed by 15%Ni/EGA3 contributed to the excellent conversion of glycerol and product yield (i.e., H_2 and Co), when compared to catalyst with other Ni metal loading. 15%Ni/EGA3 catalyst had the highest concentration of surface O^{2-} basic sites compared to the other catalysts. This surface O^{2-} accelerated the adsorption process of CO_2 molecule. Abdullah et al. [68] and Liu et al. [69] also found that the catalyst's basic sites could enhanced the adsorption of acidic CO_2 molecules.

The results from this study are strongly consistent with results from existing literature by Arif et al. [7], Tavanarad et al. [19] and Harun et al. [51] where 15%Ni loading is selected as the ideal amount of Ni to be employed for the glycerol reforming reaction. For instance, the study by Tavanarad et al. [19] using Ni/Al_2O_3 catalyst revealed that glycerol conversion increased in the order: 5%, 10%, 20%, 15% with the 15% Ni/Al_2O_3 catalyst having glycerol conversion of approximately 80% at 700 °C.

(d) Glycerol dry reforming over 20% Ni/EGA3

Ni has very high tendencies to crack C–H bonds; therefore, it is expected that as Ni loading increases from 15% to 20%, the catalytic performance should reasonably increase since more hydrocarbons are being converted. This was not the case for the 20%Ni/EGA3 because the quality of metal-support interaction significantly dropped. When 20% Ni loading was employed, results demonstrated that the increment in Ni loading from 15% to 20% varied inversely with the catalyst performance. At 20% Ni loading, the glycerol conversion, H_2 yield and CO conversion were 37%, 24% and 18%, respectively. During the catalyst synthesis, the amount of Ni nanoparticles outnumbered the active support surface area available for metal-support interaction. Therefore, the excess Ni metals agglomerate and form larger particles which do not support uniform dispersion. The agglomerated Ni particles caused by insufficient support surface (due to excess supply of 20%Ni) resulted in the sintering of the tightly bonded Ni particles (agglomerated particles) at high reaction temperature. Metals sintering leads to catalyst deactivation and drop in performance. This is evident as TEM images shown in Fig. 4(e), where visibly larger Ni particles with low dispersion can be observed. The metal-support interaction can be judged to be low because the dispersion is poor due to high rate of agglomeration of the metal particles. However, result from the XRD in Fig. 3 reveals that at 20% Ni loading the Ni species had the most intense peaks, these had no effect on the performance due to poor interaction existing between metals and support. Also, at 20%Ni/EGA3, the reduction of NiO was lower while that of spinel $NiAl_2O_4$ was at its highest probably due to weaker metal-support interaction and lower thermal stability when compared to 15%Ni/EGA3. It should be noted that for 20%Ni/EGA3, deactivation of catalyst resulting from accumulation of carbon deposits still occurred over time but deactivation due to metal agglomeration and sintering was prevalent.

Few researchers have employed 20%Ni loading for glycerol dry reforming [63,70]. Lee et al. [70] used a different kind of support (cement clinker) for GDR and observed that 20% Ni loading had the best performance in GDR when compared with 5%, 10%, 15% and 20%. However, it is worth mentioning that whisker and graphitic carbon type were observed during the carbon study of the spent 20%Ni catalysts. Therefore, the best metal loading for a given catalyst primarily depends on

the metal's properties, specific support employed and the active surface area/pores available for interaction with the metal. However, secondary variables like the amount of carbon atoms that form the carbon chain of the hydrocarbon feedstock are also considered.

In the H_2: CO ratio plot represented in Fig. 8(d); the GDR reaction successfully produced H_2-rich syngas mixture with a ratio less than 2.0 over the whole process. The result suggests that with respect to the Fischer-Tropsch (FT) synthesis, GDR reaction is a more favorable pathway than steam reforming of glycerol because it is ideal to produce syngas with high yield of H_2.

(e) Summary of glycerol dry reforming over 5%, 10%, 15% and 20% Ni/EGA3

In summary, H_2 yield (Fig. 8(b)), and CO yield (Fig. 8(c)) increased when loading of Ni increased from 5%Ni/EGA3 to 15%Ni/EGA3. When higher loading of Ni was introduced, the Ni metallic sites played a positive role in GDR reaction where higher catalytic activity of Ni/EGA3 was achieved. Increasing the Ni metal loading favored the GDR reaction until 15%Ni/EGA3 and declined significantly at 20%Ni/EGA3 majorly because of Ni metal sintering due to agglomeration of excess Ni nanoparticles during synthesis. Studies have shown that Ni has high affinity for carbon; hence, increasing the Ni content beyond 15% (above the catalyst threshold) would mean stronger Ni-carbon interaction at the surface due to the availability of long-chain carbon to carbon bonds in glycerol. Hence, more Ni-carbon interaction means more catalyst pore blockage. This could lessen the number of active sites to activate glycerol and CO_2 reactants, leading to loss of activity. One of the crucial parts in the GDR mechanism is the formation of CH_4 as a by-product from the reaction. CH_4 is produced on the surface of catalyst while the activation of CO_2 mainly happens on the support's surfaces. Thus, the competing reaction between CH_4 formation and CO_2 activation can hinder the reactant's conversion.

Furthermore, the highest glycerol conversion of 42.1% was achieved over 15%Ni/EGA3 catalyst while H_2 and CO yield of 29% and 23% respectively were produced. 15%Ni/EGA3 possesses the highest catalytic activity due to the increase in the number of Ni metal active sites that strongly optimizes the metal-support interaction. The addition of Ni in the EGA3 support framework can potentially improve the interaction between Ni and EGA3 and further enhance their catalytic performance in GDR reaction. Several literatures have also supported that the interaction between support and metal plays a vital role in achieving excellent catalytic performance. Zhang et al. [71] mentioned that the strong interaction between metals and support materials promotes better catalyst's stability and catalytic activity, while Jabbour et al. [72] reported that the increase in the catalytic activity is associated with the amount of active site.

Therefore, results from this study strongly suggests that an excellent catalytic performance by 15%Ni/EGA3 can be credited to the adequate/high accessibility of metal active sites and good support materials which favours an optimized interaction between reactants and catalyst.

Effect of reaction temperature on GDR reaction

The effect of reaction temperature was conducted at various CGR ratios (0.5, 1, 2, 3, 4, 5) and temperature ranging from 600 °C to 900 °C. 15%Ni/EGA3 catalyst was employed for all the reforming reactions carried out. Fig. 9 represents the glycerol conversion in the order (highest to lowest); CGR 1 > CGR 0.5 > CGR 2 > CGR 3 > CGR 4 > CGR 5. From the result, 15%Ni/EGA3 catalyst exhibited the best conversion of glycerol at higher temperature. One of the reasons for the slight differences in conversion as temperature increases is the dominance of various side reactions at different reaction temperature.

The conversion obtained at 600 °C, 700 °C, 800 °C, and 900 °C were 50%, 53% 56%, and 55%, respectively. It was observed that although these differences are minimal, there is a direct relationship between temperature and glycerol conversion which is coherent with the Arrhenius characteristics. The increment in reactant conversion was majorly due to the endothermic reaction of GDR and the Arrhenius reaction characteristic. 15%Ni/EGA3 catalysts exhibited greater conversions of glycerol than other catalysts due to its better ability to resist coking.

From the result, glycerol conversion peaks at 800 °C and drops slightly when the temperature is increased to 900 °C, for all synthesized catalysts. This is due to the dominance of the thermodynamically favored glycerol cracking as against the Boudouard reaction (BR) which is less likely to occur at high reaction temperature [73,74]. Besides, with respect to the catalyst, there is a reduction in the surface area of EGA3 support due to sintering at the support's surface at 900 °C. This could break the metal-support bonds and therefore limit the reaction. Thus, 800 °C was chosen as the best reaction temperature for the GDR reaction.

Post-reaction characterizations

(a) Transmission electron microscopy

Fig. 10(a)–(e) represents the surface morphologies of all EGA3 supported spent catalysts after 8 h GDR reaction. A small dark spot represents the Ni metal, a bigger dark spot represents carbon, and the grey area represents EGA3 support. Nanofilament type carbon (FC) and encapsulated type carbon (EC) were detected for all the spent catalyst as illustrated in Fig. 10(a)–(e) after GDR reforming reaction. For the TEM image of the spent 5%Ni/EGA3, 10%Ni/EGA3, 15%Ni/EGA3 and 20%Ni/EGA3 (i.e., Fig. 10(a)–(d)), larger dark spots are observed over the EGA3 support, resulting in larger size of the particles (around 13.7 nm, 13.8 nm, 13.11 nm, and 13.22 nm respectively). The larger dark spot is linked to the carbon attack on the Ni particle. However, the Ni particle size for 15%Ni/EGA3 and 20%Ni/EGA3 catalysts were lower than the other catalysts as represented in Fig. 10(c) and (d), respectively. This means that the addition of more Ni allowed for better Ni-EGA3 interaction and better conversion, suggesting that the increase in Ni loading created fine and narrow Ni particle size distribution on EGA3. This agrees with the BET analyses (i.e., refer to supplementary data for the pore size distribution data). The crystallite size and the carbon formation reduced in the following order: 5%Ni/EGA3 > 10%Ni/EGA3 > 20%Ni/

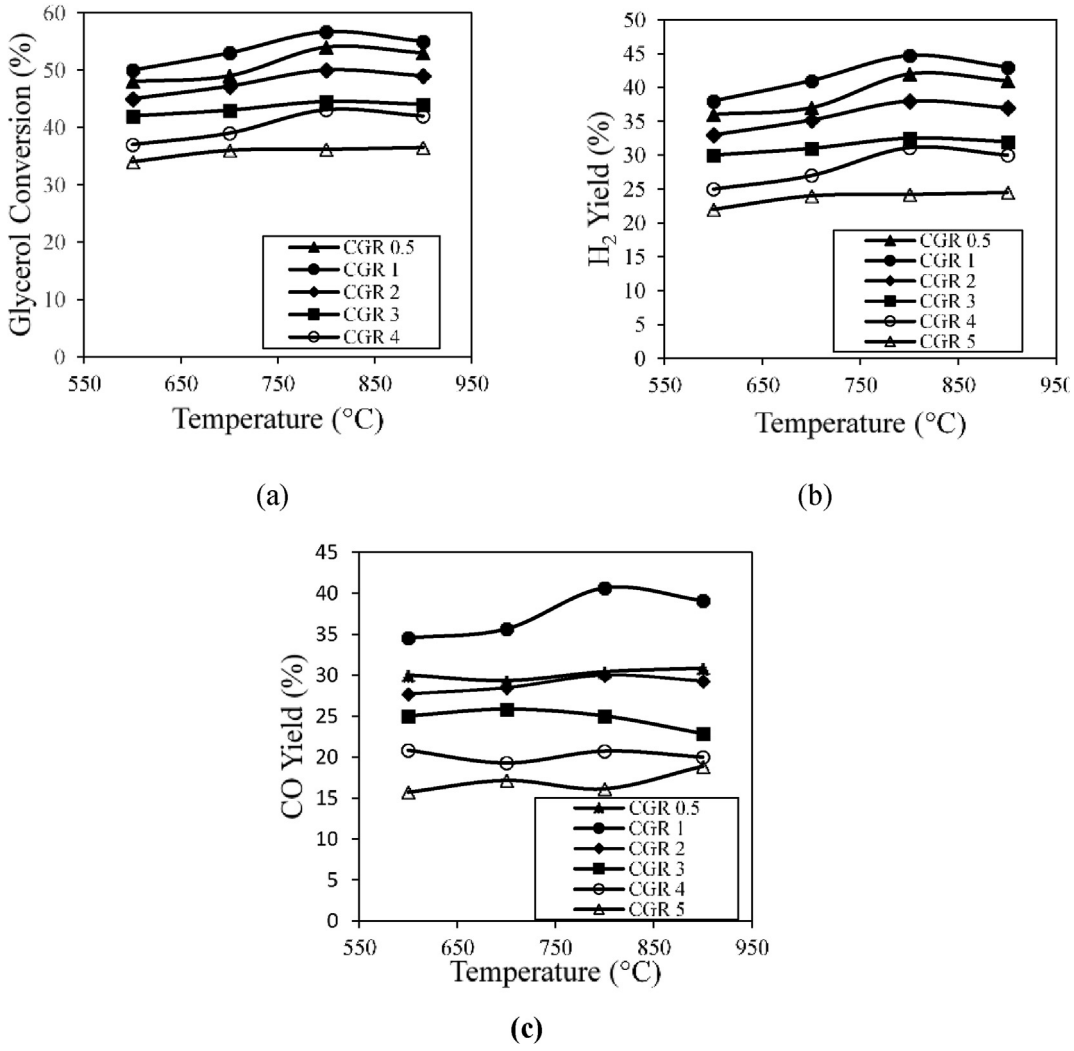

Fig. 9 – Effect of temperature on (a)Glycerol conversion, (b)H_2 yield, and (c)CO yield.

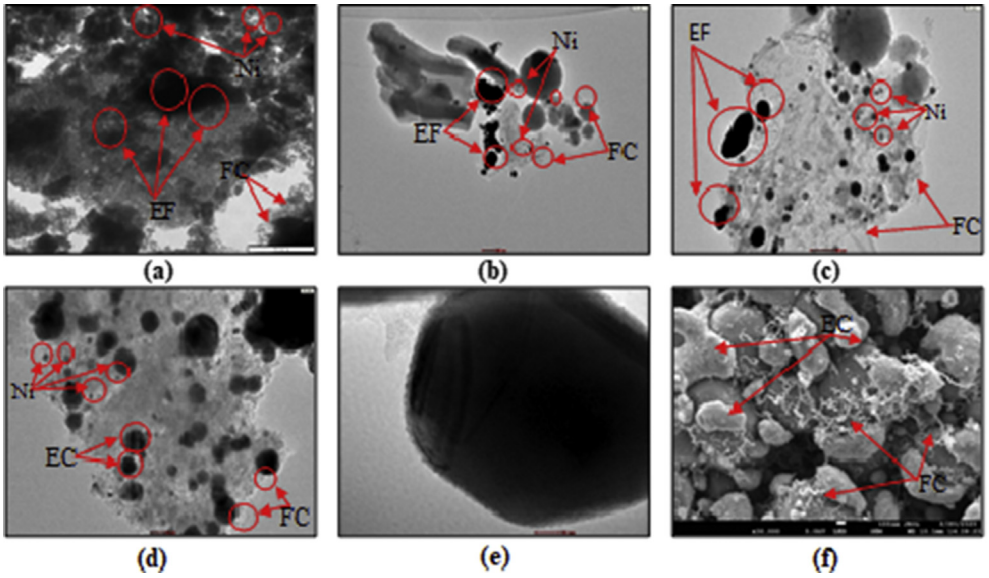

Fig. 10 – TEM image of spent (a)5%Ni/EGA3, (b)10%Ni/EGA3, (c)15%Ni/EGA3 and (d)20%Ni/EGA3, (e)EGA3, (f) FESEM image of FC type carbon.

EGA3 > 15%Ni/EGA3, which can directly be associated with the strength of Ni-EGA as shown in the TPR analysis.

Therefore, strong Ni-EGA3 interaction exhibited by 15%Ni/EGA3 reveals its ability to resist Ni sintering better than other catalysts. Earlier, filamentous carbon was reported to consist of a hollow inner channel that can aid easy gasification with CO_2. This could negatively impact the catalytic performance during the reaction [61]. Djinovic et al. [62] and Yang et al. [63] reported that the spent catalyst of Ni/Al_2O_3 possessed a huge amount of filamentous carbon, thus, inferring that the addition of Ni was able to excite the formation of filamentous carbon. The presence of filamentous carbon and encapsulated carbon in GDR using Ni/Al_2O_3 catalyst was also reported by Harun et al. [39]. The FESEM image (i.e., Fig. 10(f)) represents a clear version of filamentous carbon and encapsulated carbon on the catalyst's surface.

(b) Temperature programmed oxidation

The TPO was conducted to quantify the amount of carbon formed in 8 h GDR reaction. The weight loss and derivative weight profile are represented in Fig. 11. The total weight loss follows the order of 5%Ni/EGA3 > 10%Ni/EGA3 > 20%Ni/EGA3 > 15%Ni/EGA3. In the derivative weight profile, three main peaks are seen between 200 and 550 °C. The initial weight loss (<250 °C) represents the loss of humidity or water content. Meanwhile, peak presence within 300–400 °C represents the oxidation of carbon deposited on the catalyst's surface [75]. Another peak found at high oxidation temperature (>400 °C) was assigned to graphitic oxidation, which represents the deactivation of Ni/EGA3.

Based on literature, carbon can be formed in GDR via various side reactions [12]. It was also observed that spent 15% Ni/EGA3 catalyst had smaller particle size than that of spent 5%Ni/EGA3. This suggests that the carbon formation was more obvious in the spent 5%Ni/EGA3 because of the weak metal-support interaction. The larger particle size was due to accumulation of carbon on the Ni species at the surface. The smaller particle size of the spent 15%Ni/EGA3 was due to the more effective cleansing mechanism of carbon at the surface. Besides, the strong basic sites of 15%Ni/EGA3 supplied more oxygen surface, which prevented the deposition of carbon.

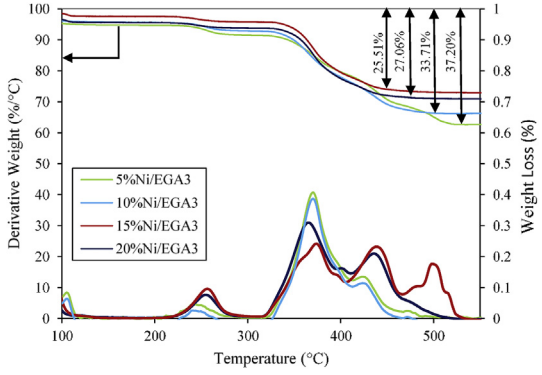

Fig. 11 – TPO profile and weight loss of spent catalyst at T = 700 °C, WHSV = 3.6 × 10^{-4} ml g^{-1} h^{-1} STP and CGR of 1.

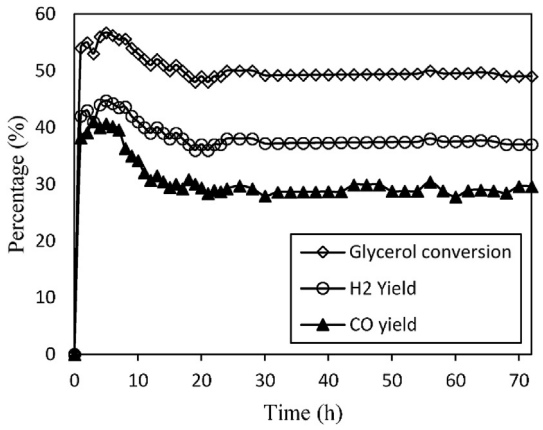

Fig. 12 – TOS profile of glycerol conversion at 15%Ni/EGA3, CGR of 1 and T = 800 °C.

Wang et al. [76] concluded that the reduction in carbon formation was related to the metal dispersion on the support's surface. Poor dispersion of Ni particle in the 20%Ni/EGA3 catalyst compared to the 15%Ni/EGA3 catalyst can be linked to metal agglomeration. The agglomerated metals occupied the catalyst's active sites thereby lowering the overall number of active sites to interact with the reactants. Lower intensity of graphite peak for 20%Ni/EGA3 catalyst supports this explanation. Hence, it can be concluded that uniform Ni metal dispersion on the EGA3 surface inhibits the rate of carbon formation during the GDR and simultaneously improves the catalytic activity and stability, which correlates with conclusions reached in previous studies [19,64]. The result infers that the incorporation of Ni on the EGA3 efficiently reduce the formation of carbon because of the numerous advantages (strong basic attributes and high oxygen vacancies) exhibited by the synthesized Ni catalyst supported on EGA3 from aluminum dross.

Longevity study

The longevity study was conducted using the best catalyst (15%/NiEGA3) and reaction condition of CGR of 1, and reaction temperature of 800 °C. As shown in Fig. 12, an initial sharp drop was observed for glycerol conversion, H_2 yield, and CO yield. The glycerol conversion declined from about 56.7% to 49% after 30 h, and then remained stable until 72 h TOS. Within the TOS, excess carbon likely enveloped the catalyst's active metal sites, thereby lowering the catalytic activity. Overall, the glycerol conversion, H_2 yield and CO yield peaked at about 56.7%, 44.7% and 40.6%, respectively. The good interaction between Ni and EGA enhanced the catalyst's stability in GDR reaction for 72 h TOS.

Conclusions

The utilization of AD waste for the preparation of γ-Al_2O_3 as catalyst support in GDR reaction has been investigated in this study. Firstly, Al_2O_3 was prepared by three different extraction techniques and it was found that the yield and BET surface area increased in the order EA3 < EA2 < EA1. EA1 was prepared

by acid leaching with ammonia precipitation technique and, was found to have the best purity (100%) and specific surface area (163.51 m^2 g^{-1}) at 800 °C calcination temperature. The introduction of ultrasonication process during the extraction technique enhance the separation process to achieve higher BET surface area and purity. Prior to its application as catalyst support, EA1 was calcined at different calcination temperature to ensure the stability of the EA phase during high reaction temperature. EGA3 produced with the highest specific surface area (267.5 m^2 g^{-1}) at 800 °C calcination temperature was selected to be used as catalyst support in GDR reaction. Higher calcination temperature led to a reduction of BET surface area due to sintering of support surface. EGA3 produced with the highest specific surface area (267.5 m^2 g^{-1}) at 800 °C calcination temperature was selected to be used as catalyst support in GDR reaction. Four different loadings of Ni (5 wt%, 10 wt%, 15 wt% and 20 wt%) were used to synthesize the Ni/EGA3 catalyst via the ultrasonicated impregnation method before evaluation in GDR reaction. The incorporation of Ni reduced both pore diameter and BET surface area of the synthesized catalyst, which was linked to enhanced Ni dispersion and reduction in crystallite size of the EGA3 support. The reactant conversions increased in the order; 5%Ni/EGA3 > 10%Ni/EGA3 > 20%Ni/EGA3 > 15%Ni/EGA3, with the later achieving the highest glycerol conversion of about 56.7% at 800 °C reaction temperature. The 15%Ni/EGA3 catalyst had an excellent catalytic performance when compared to other catalysts due to its strong basic site and high binding energy. H_2-TPR analysis proved that the large crystallite size of 20%Ni/EGA3 weakened the metal-support interaction. TEM and TPO analyses on the spent catalysts showed the existence of EC and FC carbon type after 8 h GDR reaction. Addition of high Ni loading (until 15 wt%) effectively reduced the formation of carbon since TPO results revealed decrease in the amount of carbon in the order; 5%Ni/EGA3 > 10%Ni/EGA3 > 20%Ni/EGA3 > 15%Ni/EGA3. Therefore, γ-Al_2O_3 from AD can be very effective as catalyst support for Ni-based catalyst just like the conventional Al_2O_3 support. The superior performance achieved by 15%Ni/EGA3 catalyst in GDR was due to its better Ni metals dispersion on the EGA3 surface and strong interaction between Ni-EGA3 compared to other catalyst synthesized in this study.

Declaration of competing interest

The authors declare that they have no known competing financial interests or personal relationships that could have appeared to influence the work reported in this paper.

Acknowledgements

The authors would like to thank Ministry of Higher Education, Malaysia for awarding Fundamental Research Grant Scheme with vote number FRGS/1/2018/TK02/UMP/02/12 (RDU190197) and Universiti Malaysia Pahang (RDU 1803118 and PGRS1903121) for financial support.

Appendix A. Supplementary data

Supplementary data to this article can be found online at https://doi.org/10.1016/j.ijhydene.2021.03.162.

REFERENCES

[1] Mehrpooya M, Ghorbani B, Abedi H. Biodiesel production integrated with glycerol steam reforming process, solid oxide fuel cell (SOFC) power plant. Energy Convers Manag 2020;206:112467. https://doi.org/10.1016/j.enconman.2020.112467.

[2] Shokrollahi Yancheshmeh M, Alizadeh Sahraei O, Aissaoui M, Iliuta MC. A novel synthesis of $NiAl_2O_4$ spinel from a Ni-Al mixed-metal alkoxide as a highly efficient catalyst for hydrogen production by glycerol steam reforming. Appl Catal B Environ 2020;265:118535. https://doi.org/10.1016/j.apcatb.2019.118535.

[3] Wang S, Wang J, Sun P, Xu L, Okoye PU, Li S, et al. Disposable baby diapers waste derived catalyst for synthesizing glycerol carbonate by the transesterification of glycerol with dimethyl carbonate. J Clean Prod 2019;211:330–41. https://doi.org/10.1016/j.jclepro.2018.11.196.

[4] Huang C, Xu C, Wang B, Hu X, Li J, Liu J, et al. High production of syngas from catalytic steam reforming of biomass glycerol in the presence of methane. Biomass Bioenergy 2018;119:173–8. https://doi.org/10.1016/j.biombioe.2018.05.006.

[5] Bac S, Keskin S, Avci AK. Recent advances in materials for high purity H_2 production by ethanol and glycerol steam reforming. Int J Hydrogen Energy 2020;45:34888–917. https://doi.org/10.1016/j.ijhydene.2019.11.237.

[6] Dias FPF, Fernandes IT, Bueno AV, Rocha PAC, de Oliveira MLM. Exergy analysis of glycerol steam reforming in a heat recovery reactor. Int J Hydrogen Energy 2021;46:8995–9007. https://doi.org/10.1016/j.ijhydene.2020.12.215.

[7] Mohd Arif NN, Abidin SZ, Osazuwa OU, Azizan MT, Taufiq-Yap YH. Hydrogen production via CO_2 dry reforming of glycerol over ReNi/CaO catalysts. Int J Hydrogen Energy 2019;44:20857–71. https://doi.org/10.1016/J.IJHYDENE.2018.06.084.

[8] Siew KW, Lee HC, Gimbun J, Cheng CK. Characterization of La-promoted Ni/Al_2O_3 catalysts for hydrogen production from glycerol dry reforming. J Energy Chem 2014;23:15–21. https://doi.org/10.1016/S2095-4956(14)60112-1.

[9] Pakhare D, Spivey J. A review of dry (CO_2) reforming of methane over noble metal catalysts. Chem Soc Rev 2014;43:7813–37. https://doi.org/10.1039/c3cs60395d.

[10] Kale GR, Kulkarni BD. Thermodynamic analysis of dry autothermal reforming of glycerol. Fuel Process Technol 2010;91:520–30. https://doi.org/10.1016/j.fuproc.2009.12.015.

[11] Bac S, Say Z, Kocak Y, Ercan KE, Harfouche M, Ozensoy E, et al. Exceptionally active and stable catalysts for CO_2 reforming of glycerol to syngas. Appl Catal B Environ 2019;256:117808. https://doi.org/10.1016/j.apcatb.2019.117808.

[12] Bulutoglu PS, Say Z, Bac S, Ozensoy E, Avci AK. Dry reforming of glycerol over Rh-based ceria and zirconia catalysts: new insights on catalyst activity and stability. Appl Catal Gen 2018;564:157–71. https://doi.org/10.1016/j.apcata.2018.07.027.

[13] le Saché E, Pastor-Pérez L, Watson D, Sepúlveda-Escribano A, Reina TR. Ni stabilised on inorganic complex structures: superior catalysts for chemical CO_2 recycling via dry reforming of methane. Appl Catal B Environ 2018;236:458–65. https://doi.org/10.1016/j.apcatb.2018.05.051.
[14] Bastan F, Kazemeini M, Larimi A, Maleki H. Production of renewable hydrogen through aqueous-phase reforming of glycerol over Ni/Al_2O_3–MgO nano-catalyst. Int J Hydrogen Energy 2018;43:614–21. https://doi.org/10.1016/j.ijhydene.2017.11.122.
[15] Ismaila A, Chen H, Shao Y, Xu S, Jiao Y, Chen X, et al. Renewable hydrogen production from steam reforming of glycerol (SRG) over ceria-modified γ-alumina supported Ni catalyst. Chin J Chem Eng 2020;28:2328–36. https://doi.org/10.1016/j.cjche.2020.06.025.
[16] Bian Z, Das S, Wai MH, Hongmanorom P, Kawi S. A review on bimetallic nickel-based catalysts for CO_2 reforming of methane. ChemPhysChem 2017;18:3117–34. https://doi.org/10.1002/cphc.201700529.
[17] Bepari S, Kuila D. Steam reforming of methanol, ethanol and glycerol over nickel-based catalysts-A review. Int J Hydrogen Energy 2020;45:18090–113. https://doi.org/10.1016/j.ijhydene.2019.08.003.
[18] Chong CC, Cheng YW, Setiabudi HD, Ainirazali N, Vo DVN, Abdullah B. Dry reforming of methane over Ni/dendritic fibrous SBA-15 (Ni/DFSBA-15): optimization, mechanism, and regeneration studies. Int J Hydrogen Energy 2020;45:8507–25. https://doi.org/10.1016/j.ijhydene.2020.01.056.
[19] Tavanarad M, Meshkani F, Rezaei M. Production of syngas via glycerol dry reforming on Ni catalysts supported on mesoporous nanocrystalline Al_2O_3. J CO_2 Util 2018;24:298–305. https://doi.org/10.1016/j.jcou.2018.01.009.
[20] Lima DS, Calgaro CO, Perez-Lopez OW. Hydrogen production by glycerol steam reforming over Ni based catalysts prepared by different methods. Biomass Bioenergy 2019;130:105358. https://doi.org/10.1016/j.biombioe.2019.105358.
[21] Ramesh S, Yang EH, Jung JS, Moon DJ. Copper decorated perovskite an efficient catalyst for low temperature hydrogen production by steam reforming of glycerol. International journal of hydrogen energy, vol. 40. Elsevier Ltd; 2015. p. 11428–35. https://doi.org/10.1016/j.ijhydene.2015.02.013.
[22] Sanchez EA, Comelli RA. Hydrogen production by glycerol steam-reforming over nickel and nickel-cobalt impregnated on alumina. International journal of hydrogen energy, vol. 39. Elsevier Ltd; 2014. p. 8650–5. https://doi.org/10.1016/j.ijhydene.2013.12.067.
[23] Goula MA, Charisiou ND, Papageridis KN, Delimitis A, Pachatouridou E, Iliopoulou EF. Nickel on alumina catalysts for the production of hydrogen rich mixtures via the biogas dry reforming reaction: influence of the synthesis method. Int J Hydrogen Energy 2015;40:9183–200. https://doi.org/10.1016/j.ijhydene.2015.05.129.
[24] Roslan NA, Abidin SZ, Ideris A, Vo DVN. A review on glycerol reforming processes over Ni-based catalyst for hydrogen and syngas productions. Int J Hydrogen Energy 2020;45:18466–89. https://doi.org/10.1016/j.ijhydene.2019.08.211.
[25] Aziz MAA, Setiabudi HD, Teh LP, Annuar NHR, Jalil AA. A review of heterogeneous catalysts for syngas production via dry reforming. J Taiwan Inst Chem Eng 2019;101:139–58. https://doi.org/10.1016/j.jtice.2019.04.047.
[26] Chong CC, Cheng YW, Bahari MB, Teh LP, Abidin SZ, Setiabudi HD. Development of nanosilica-based catalyst for syngas production via CO_2 reforming of CH_4: a review. Int J Hydrogen Energy 2021;46:24687–708. https://doi.org/10.1016/j.ijhydene.2020.01.086.
[27] Charisiou ND, Papageridis KN, Tzounis L, Sebastian V, Hinder SJ, Baker MA, et al. Ni supported on CaO-MgO-Al_2O_3 as a highly selective and stable catalyst for H_2 production via the glycerol steam reforming reaction. Int J Hydrogen Energy 2019;44:256–73. https://doi.org/10.1016/j.ijhydene.2018.02.165.
[28] El Doukkali M, Iriondo A, Miletic N, Cambra JF, Arias PL. Hydrothermal stability improvement of NiPt-containing Γ-Al_2O_3 catalysts tested in aqueous phase reforming of glycerol/water mixture for H_2 production. Int J Hydrogen Energy 2017;42:23617–30. https://doi.org/10.1016/j.ijhydene.2017.04.218.
[29] Farooqi AS, Al-Swai BM, Ruslan FH, Mohd Zabidi NA, Saidur R, Syed Muhammad SAF ad, et al. Catalytic conversion of greenhouse gases (CO_2 and CH_4) to syngas over Ni-based catalyst: effects of Ce-La promoters. Arab J Chem 2020;13:5740–9. https://doi.org/10.1016/j.arabjc.2020.04.012.
[30] Lee J, Jang EJ, Kwak JH. Acid-base properties of Al_2O_3: effects of morphology, crystalline phase, and additives. J Catal 2017;345:135–48. https://doi.org/10.1016/j.jcat.2016.11.025.
[31] Son IH, Kwon S, Park JH, Lee SJ. High coke-resistance $MgAl_2O_4$ islands decorated catalyst with minimizing sintering in carbon dioxide reforming of methane. Nanomater Energy 2016;19:58–67. https://doi.org/10.1016/j.nanoen.2015.11.007.
[32] Papageridis KN, Siakavelas G, Charisiou ND, Avraam DG, Tzounis L, Kousi K, et al. Comparative study of Ni, Co, Cu supported on γ-alumina catalysts for hydrogen production via the glycerol steam reforming reaction. Fuel Process Technol 2016;152:156–75. https://doi.org/10.1016/j.fuproc.2016.06.024.
[33] Bobadilla LF, Penkova A, Romero-Sarria F, Centeno MA, Odriozola JA. Influence of the acid-base properties over NiSn/MgO-Al_2O_3 catalysts in the hydrogen production from glycerol steam reforming. International journal of hydrogen energy, vol. 39. Elsevier Ltd; 2014. p. 5704–12. https://doi.org/10.1016/j.ijhydene.2014.01.136.
[34] Hong JP, Wang J, Chen HY, De Sun B, Li JJ, Chen C. Process of aluminum dross recycling and life cycle assessment for Al-Si alloys and brown fused alumina. Trans Nonferrous Metals Soc China 2010;20:2155–61. https://doi.org/10.1016/S1003-6326(09)60435-0.
[35] Tripathy AK, Mahalik S, Sarangi CK, Tripathy BC, Sanjay K, Bhattacharya IN. A pyro-hydrometallurgical process for the recovery of alumina from waste aluminium dross. Miner Eng 2019;137:181–6. https://doi.org/10.1016/j.mineng.2019.04.009.
[36] Mahinroosta M, Allahverdi A. Hazardous aluminum dross characterization and recycling strategies: a critical review. J Environ Manag 2018;223:452–68. https://doi.org/10.1016/j.jenvman.2018.06.068.
[37] Meshram A, Singh KK. Recovery of valuable products from hazardous aluminum dross: a review. Resour Conserv Recycl 2018;130:95–108. https://doi.org/10.1016/j.resconrec.2017.11.026.
[38] Abd-El-Raoof F, Tawfik A, Komarneni S, Ahmed SE. Hydrotalcite and hydrocalumite as resources from waste materials of concrete aggregate and Al-dross by microwave-hydrothermal process. Construct Build Mater 2019;207:10–6. https://doi.org/10.1016/j.conbuildmat.2019.02.105.
[39] Mailar G, N SR, B.M S, D.S M, Hiremath P, K J. Investigation of concrete produced using recycled aluminium dross for hot weather concreting conditions. Resour Technol 2016;2:68–80. https://doi.org/10.1016/j.reffit.2016.06.006.
[40] Ibarra Castro MN, Almanza Robles JM, Cortés Hernández DA, Escobedo Bocardo JC, Torres Torres J. Development of mullite/zirconia composites from a mixture of aluminum dross and zircon. Ceram Int 2009;35:921–4. https://doi.org/10.1016/j.ceramint.2008.03.006.
[41] Nguyen TTN, Song SJ, Lee MS. Development of a hydrometallurgical process for the recovery of pure alumina

from black dross and synthesis of magnesium spinel. J Mater Res Technol 2020;9:2568–77. https://doi.org/10.1016/j.jmrt.2019.12.087.
[42] Zhu X, Jin Q, Ye Z. Life cycle environmental and economic assessment of alumina recovery from secondary aluminum dross in China. J Clean Prod 2020;277:123291. https://doi.org/10.1016/j.jclepro.2020.123291.
[43] Saravanakumar R, Ramachandran K, Laly LG, Ananthapadmanabhan PV, Yugeswaran S. Plasma assisted synthesis of γ-alumina from waste aluminium dross. Waste Manag 2018;77:565–75. https://doi.org/10.1016/j.wasman.2018.05.005.
[44] Roslan NA, Abidin SZ, Nasir NS, Chin SY, Taufiq-Yap YH. Extracted γ-Al_2O_3 from aluminum dross as a catalyst support for glycerol dry reforming reaction. Mater Today Proc 2021. https://doi.org/10.1016/j.matpr.2020.09.390.
[45] How LF, Islam A, Jaafar MS, Taufiq-Yap YH. Extraction and characterization of Γ-alumina from waste aluminium dross. Waste Biomass Valorization 2017;8:321–7. https://doi.org/10.1007/s12649-016-9591-4.
[46] Mahinroosta M, Allahverdi A. A promising green process for synthesis of high purity activated-alumina nanopowder from secondary aluminum dross. J Clean Prod 2018;179:93–102. https://doi.org/10.1016/j.jclepro.2018.01.079.
[47] Miskufova A, Petranikova M, Kovacs M, Havlik T, Orac D, Briancin J. Leaching of aluminium dross in alkaline solution. Proc - Eur Metall Conf EMC 2009;2009(4):1339–50.
[48] Mahinroosta M, Allahverdi A, Dong P, Bassim N. Green template-free synthesis and characterization of mesoporous alumina as a high value-added product in aluminum black dross recycling strategy. J Alloys Compd 2019;792:161–9. https://doi.org/10.1016/j.jallcom.2019.04.009.
[49] Lazaro A, Brouwers HJH, Quercia G, Geus JW. The properties of amorphous nano-silica synthesized by the dissolution of olivine. Chem Eng J 2012;211–212:112–21. https://doi.org/10.1016/j.cej.2012.09.042.
[50] Smoljan CS, Crawford JM, Carreon MA. Mesoporous microspherical NiO catalysts for the deoxygenation of oleic acid. Catal Commun 2020;143:106046. https://doi.org/10.1016/j.catcom.2020.106046.
[51] Harun N, Abidin SZ, Osazuwa OU, Taufiq-Yap YH, Azizan MT. Hydrogen production from glycerol dry reforming over Ag-promoted Ni/Al_2O_3. Int J Hydrogen Energy 2019;44:213–25. https://doi.org/10.1016/j.ijhydene.2018.03.093.
[52] Irshad HM, Hakeem AS, Ahmed BA, Ali S, Ali S, Ali S, et al. Effect of Ni content and Al_2O_3 particle size on the thermal and mechanical properties of Al_2O_3/Ni composites prepared by spark plasma sintering. Int J Refract Metals Hard Mater 2018;76:25–32. https://doi.org/10.1016/j.ijrmhm.2018.05.010.
[53] Hindryawati N, Maniam GP, Karim MR, Chong KF. Transesterification of used cooking oil over alkali metal (Li, Na, K) supported rice husk silica as potential solid base catalyst. Int J Eng Sci Technol 2014;17:95–103. https://doi.org/10.1016/j.jestch.2014.04.002.
[54] Hardiman KM, Cooper CG, Adesina AA, Lange R. Post-mortem characterization of coke-induced deactivated alumina-supported Co-Ni catalysts. Chem Eng Sci 2006;61:2565–73. https://doi.org/10.1016/j.ces.2005.11.021.
[55] Shafiee P, Alavi SM, Rezaei M. Mechanochemical synthesis method for the preparation of mesoporous Ni–Al_2O_3 catalysts for hydrogen purification via CO_2 methanation. J Energy Inst 2021;96:1–10. https://doi.org/10.1016/j.joei.2021.01.015.
[56] Takenaka S, Shimizu T, Otsuka K. Complete removal of carbon monoxide in hydrogen-rich gas stream through methanation over supported metal catalysts. Int J Hydrogen Energy 2004;29:1065–73. https://doi.org/10.1016/j.ijhydene.2003.10.009.
[57] Arcotumapathy V, Vo DVN, Chesterfield D, Tin CT, Siahvashi A, Lucien FP, et al. Catalyst design for methane steam reforming. Appl Catal Gen 2014;479:87–102. https://doi.org/10.1016/j.apcata.2014.04.020.
[58] Peck MA, Langell MA. Comparison of nanoscaled and bulk NiO structural and environmental characteristics by XRD, XAFS, and XPS. Chem Mater 2012;24:4483–90. https://doi.org/10.1021/cm300739y.
[59] He S, He S, Zhang L, Li X, Wang J, He D, et al. Hydrogen production by ethanol steam reforming over Ni/SBA-15 mesoporous catalysts: effect of Au addition. Catal Today 2015;258:162–8. https://doi.org/10.1016/j.cattod.2015.04.031.
[60] Lee HC, Siew KW, Gimbun J, Cheng CK. Synthesis and characterisation of cement clinker-supported nickel catalyst for glycerol dry reforming. Chem Eng J 2014;255:245–56. https://doi.org/10.1016/j.cej.2014.06.044.
[61] Selvarajah K, Phuc NHH, Abdullah B, Alenazey F, Vo DVN. Syngas production from methane dry reforming over Ni/Al_2O_3 catalyst. Res Chem Intermed 2016;42:269–88. https://doi.org/10.1007/s11164-015-2395-5.
[62] Dieuzeide ML, Iannibelli V, Jobbagy M, Amadeo N. Steam reforming of glycerol over Ni/Mg/γ-Al_2O_3 catalysts. Effect of calcination temperatures. International journal of hydrogen energy, vol. 37. Pergamon; 2012. p. 14926–30. https://doi.org/10.1016/j.ijhydene.2011.12.086.
[63] Siew KW, Lee HC, Gimbun J, Chin SY, Khan MR, Taufiq-Yap YH, et al. Syngas production from glycerol-dry(CO_2) reforming over La-promoted Ni/Al_2O_3 catalyst. Renew Energy 2015;74:441–7. https://doi.org/10.1016/j.renene.2014.08.048.
[64] Oemar U, Kathiraser Y, Mo L, Ho XK, Kawi S. CO2 reforming of methane over highly active La-promoted Ni supported on SBA-15 catalysts: mechanism and kinetic modelling. Catal Sci Technol 2016;6:1173–86. https://doi.org/10.1039/c5cy00906e.
[65] Luisetto I, Tuti S, Battocchio C, Lo Mastro S, Sodo A. Ni/CeO_2–Al_2O_3 catalysts for the dry reforming of methane: the effect of $CeAlO_3$ content and nickel crystallite size on catalytic activity and coke resistance. Appl Catal Gen 2015;500:12–22. https://doi.org/10.1016/J.APCATA.2015.05.004.
[66] Koc S, Avci AK. Reforming of glycerol to hydrogen over Ni-based catalysts in a microchannel reactor. Fuel Process Technol 2017;156:357–65. https://doi.org/10.1016/j.fuproc.2016.09.019.
[67] Feng P, Huang K, Xu Q, Qi W, Xin S, Wei T, et al. Ni supported on the CaO modified attapulgite as catalysts for hydrogen production from glycerol steam reforming. Int J Hydrogen Energy 2020;45:8223–33. https://doi.org/10.1016/j.ijhydene.2020.01.013.
[68] Abdullah N, Ainirazali N, Chong CC, Razak HA, Setiabudi HD, Chin SY, et al. Effect of Ni loading on SBA-15 synthesized from palm oil fuel ash waste for hydrogen production via CH_4 dry reforming. Int J Hydrogen Energy 2020;45:18411–25. https://doi.org/10.1016/J.IJHYDENE.2019.09.093.
[69] Liu H, Da Costa P, Hadj Taief HB, Benzina M, Gálvez ME. Mg-promotion of Ni natural clay-supported catalysts for dry reforming of methane. RSC Adv 2018;8:19627–34. https://doi.org/10.1039/c8ra02615g.

[70] Lee HC, Siew KW, Khan MR, Chin SY, Gimbun J, Cheng CK. Catalytic performance of cement clinker supported nickel catalyst in glycerol dry reforming. J Energy Chem 2014;23:645–56. https://doi.org/10.1016/S2095-4956(14)60196-0.
[71] Zhang Q, Wang J, Ning P, Zhang T, Wang M, Long K, et al. Dry reforming of methane over Ni/SBA-15 catalysts prepared by homogeneous precipitation method. Kor J Chem Eng 2017;34:2823–31. https://doi.org/10.1007/s11814-017-0182-2.
[72] Jabbour K, El Hassan N, Casale S, Estephane J, El Zakhem H. Promotional effect of Ru on the activity and stability of Co/SBA-15 catalysts in dry reforming of methane. Int J Hydrogen Energy 2014;39:7780–7. https://doi.org/10.1016/j.ijhydene.2014.03.040.
[73] Fan MS, Abdullah AZ, Bhatia S. Catalytic technology for carbon dioxide reforming of methane to synthesis gas. ChemCatChem 2009;1:192–208. https://doi.org/10.1002/cctc.200900025.
[74] Khajenoori M, Rezaei M, Meshkani F. Dry reforming over CeO_2-promoted Ni/MgO nano-catalyst: effect of Ni loading and CH_4/CO_2 molar ratio. J Ind Eng Chem 2015;21:717–22. https://doi.org/10.1016/J.JIEC.2014.03.043.
[75] Yang W, Liu H, Li Y, Wu H, He D. CO2 reforming of methane to syngas over highly-stable Ni/SBA-15 catalysts prepared by P123-assisted method. Int J Hydrogen Energy 2016;41:1513–23. https://doi.org/10.1016/j.ijhydene.2015.11.044.
[76] Wang N, Yu X, Shen K, Chu W, Qian W. Synthesis, characterization and catalytic performance of MgO-coated Ni/SBA-15 catalysts for methane dry reforming to syngas and hydrogen. Int J Hydrogen Energy 2013;38:9718–31. https://doi.org/10.1016/j.ijhydene.2013.05.097.